

Swap-Net: A Memory-Efficient 2.5D Network for Sparse-View 3D Cone Beam CT Reconstruction

Xiaojian Xu*, Marc Klasky†, Michael T. McCann†, Jason Hu*, and Jeffrey A. Fessler*, ‡

Abstract

Reconstructing 3D cone beam computed tomography (CBCT) images from a limited set of projections is an important inverse problem in many imaging applications from medicine to inertial confinement fusion (ICF). The performance of traditional methods such as filtered back projection (FBP) and model-based regularization is sub-optimal when the number of available projections is limited. In the past decade, deep learning (DL) has gained great popularity for solving CT inverse problems. A typical DL-based method for CBCT image reconstruction is to learn an end-to-end mapping by training a 2D or 3D network. However, 2D networks fail to fully use global information. While 3D networks are desirable, they become impractical as image sizes increase because of the high memory cost. This paper proposes Swap-Net, a memory-efficient 2.5D network for sparse-view 3D CBCT image reconstruction. Swap-Net uses a sequence of novel axes-swapping operations to produce 3D volume reconstruction in an end-to-end fashion without using full 3D convolutions. Simulation results show that Swap-Net consistently outperforms baseline methods both quantitatively and qualitatively in terms of reducing artifacts and preserving details of complex hydrodynamic simulations of relevance to the ICF community.

1 Introduction

The recovery of high-quality images from limited projection measurements is fundamental in computed tomography (CT) [1]. Cone beam CT (CBCT) is a specialized imaging technique used in fields requiring detailed 3D imaging. In CBCT, an X-ray beam is projected through the 3D object onto a 2D detector. Unlike traditional CT scanners where the X-ray beam is collimated into a narrow fan shape, CBCT systems use a cone-shaped beam, allowing wider coverage of the object in a single rotation. CBCT is a valuable tool in various applications for obtaining detailed structural information [2–4].

A CBCT scanner captures 2D X-ray projections, also called radiographs, as it rotates around the target object. Computer algorithms process these projections to reconstruct a 3D volumetric image of the object. Developing fast and accurate methods for 3D CBCT image reconstruction is important in many applications [2–4]. Filtered back projection (FBP) is a classical algorithm that is computationally efficient and relatively straightforward to implement [5, 6]. However, FBP is sensitive to measurement noise and leads to artifacts when given incomplete or irregularly sampled projection data. Regularized inversion methods view CT imaging as an *inverse problem*, where the unknown object is reconstructed by combining a CT physical model and a hand-crafted regularizer [7–15]. Recently, *deep learning (DL)* methods have gained popularity in solving CBCT inverse problems [16–20]. Traditional DL methods are based on training *convolutional neural networks (CNNs)* to map the measurements or low-quality images to the desired high-quality images. *Deep model-based architectures (DMBAs)*, such as those based on deep unfolding [21, 22], have recently extended traditional DL to neural network architectures that combine the CT forward models and CNN regularizers [23–31].

*X. Xu, J. Hu, and J. A. Fessler are with the Department of Electrical Engineering & Computer Science, University of Michigan, MI 48109, USA.

†M. T. McCann and M. Klasky are with Theoretical Division, Los Alamos National Laboratory, Los Alamos, NM 87545, USA.

‡This material is based upon work supported by the Laboratory Directed Research and Development program of Los Alamos National Laboratory.

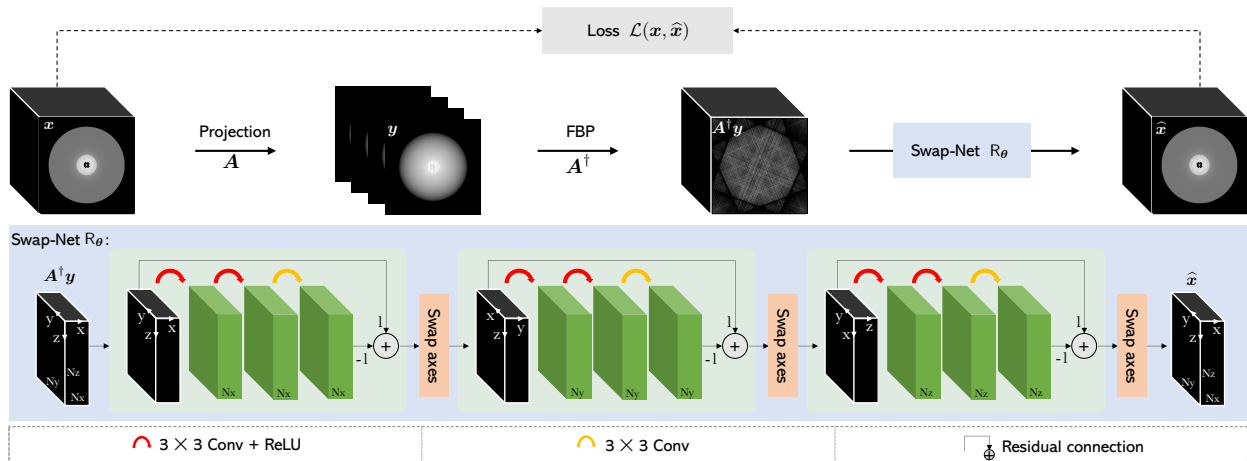


Figure 1: Overview of the proposed Swap-Net framework for training an end-to-end deep mapping for 3D CBCT image reconstruction using ICF synthetic radiographs. The Swap-Net model R_θ is implemented as a customized architecture mapping the output of FBP to the desired ground-truth 3D images. The novel axes-swapping operation in Swap-Net allows it to efficiently conduct convolution across all dimensions. The whole network is trained end-to-end in a supervised fashion.

Despite the rich literature on DL-based methodologies, direct end-to-end 3D CT reconstruction remains a challenging problem due to its high memory and computation cost. Current schemes typically use a 2D approach, where the 3D volume is divided into a series of 2D slices along one or more axes. Then each 2D slice is treated as an independent image, and a 2D neural network is applied to process each slice individually. After processing all 2D slices, the outputs are combined to reconstruct the full 3D volume. Using a 2D network for 3D reconstruction offers several advantages, including computational efficiency, ease of implementation, and compatibility with existing 2D CNN architectures and frameworks. However, it also suffers from drawbacks such as the potential loss of consistency across slices and suboptimal performance in capturing complex 3D structures compared to dedicated 3D reconstruction approaches [32, 33]. This paper addresses these issues by presenting a new network—called Swap-Net—for recovering high-quality 3D images from extreme sparse-view measurements. Distinct from the fully 3D volume-based approaches and 2D slice-based approaches, Swap-Net is developed as a 2.5D CNN where 2D convolution operations are used to extract correlations across all three dimensions of a 3D volume. The key contributions of our work are summarized as follows:

- We present a memory-efficient 2.5D network called Swap-Net to handle end-to-end 3D image reconstruction. The key component in Swap-Net is the new axes-swapping operation that helps combine information along all axes similar to 3D convolution.
- We investigated challenging sparse-view 3D CBCT image reconstruction problems with as few as 4 projection views. Moreover, we accounted for non-ideal physics including blur, scatter, and non-white noise. Simulation results demonstrate that the method can restore high-quality 3D volumes across all dimensions, outperforming baseline methods both quantitatively and qualitatively in terms of artifact-reduction and detail-preservation.
- We conducted additional investigations using Swap-Net, e.g., studying the benefits of the axis-swapping and the impact of the swapping order. Our results show that the properly chosen axis-swapping order can effectively boost the performance of the network.

The rest of this paper is organized as follows. Section 2 introduces the background and mathematical

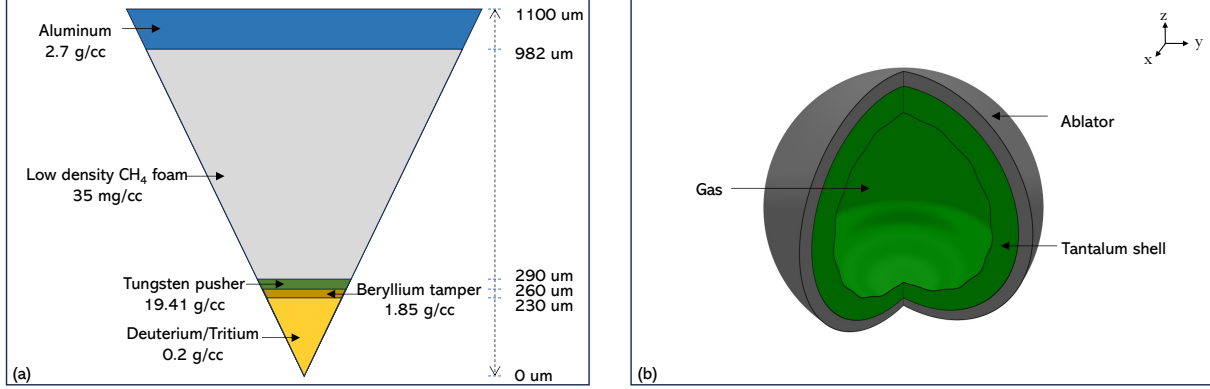


Figure 2: The ICF models: (a) A typical double-shell ICF capsule containing Deuterium/Tritium, Beryllium tamper, Tungsten pusher, low density CH_4 foam, and Aluminum. (b) A simplified representation of an ICF implosion capsule containing Deuterium/Tritium (Ablator), Tungsten pusher (Tantalum), and low density CH_4 foam (Gas) [34].

formulation of the CBCT imaging problem and discusses related work. Section 3 presents our proposed approach in detail. Section 4 explains our experimental setup, presents the results of our comparisons to other algorithms, and elaborates upon the analysis of the observations. Finally, Section 5 summarizes our work and discusses potential future directions.

2 Background

2.1 CT Inverse Problem Formulation

In CT imaging, the relationship between the unknown object $\mathbf{x} \in \mathbb{R}^n$ and the (log) projection measurements $\mathbf{y} \in \mathbb{R}^m$ is commonly expressed as a linear imaging system

$$\mathbf{y} = \mathbf{A}\mathbf{x} + \mathbf{e}, \quad (1)$$

where $\mathbf{A} \in \mathbb{R}^{m \times n}$ denotes the measurement operator (also known as the forward model or physical model) and $\mathbf{e} \in \mathbb{R}^m$ denotes the measurement noise that is sometimes statistically modeled as additive white Gaussian noise (AWGN). The AWGN formulation is a widely used approximation for various imaging systems including CT, magnetic resonance imaging (MRI), etc. [35, 36].

Scatter is another practical corruption that arises in CT imaging due to interactions between X-ray photons and objects. When X-ray photons encounter the object, some of them undergo scattering rather than being absorbed or passing straight through. Since scattered photons have undergone direction changes, they do not provide accurate information about the original object attenuation along the X-ray path. Scattered photons can reach the detector and contribute to errors that reduce the quality of the reconstructed image. Often the post-log scatter-corrupted CBCT projection measurements \mathbf{y} are modeled as

$$\mathbf{y} = -\log \left(\frac{\Phi(I_0 e^{-\mathbf{A}\mathbf{x}})}{I_0} \right), \quad (2)$$

where I_0 denotes the reference intensity from the source, Φ is a nonlinear function that models the non-ideal physics including blur and scatter corruption (see Section 4-B for details), and \log is applied pixelwise. Choices for modeling the scatter component of the function Φ in the literature include kernel convolution with the direct signal followed by Poisson noise [37, 38]. For any noise model, the goal is to reconstruct the image volume \mathbf{x} from the projection data \mathbf{y} .

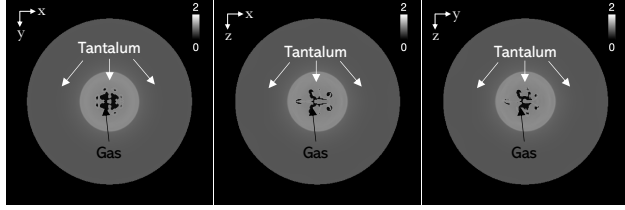


Figure 3: Central slices along each dimension of an exemplar 3D ICF object generated for an ICF double shell simulation in our dataset. The two materials that form the object, namely gas and metal, are labeled in each image. The images presented here were normalized by the mass attenuation factor to the range of $[0, 2]$ for good visualization (same in the rest of the paper).

2.2 Related Work for CT Reconstruction

As a 3D-imaging technique, CBCT imaging offers many benefits in clinical, industry, and research. However, due to factors such as computation cost, scatter, noise, limited measurements, and discrepancies in the forward operator model, significant challenges emerge when attempting to efficiently and accurately reconstruct the 3D CT images outlined in (1) and (2) [39–41]. Classical approaches tackle CT reconstruction by formulating it as a regularized optimization problem

$$\hat{\mathbf{x}} = \arg \min_{\mathbf{x} \in \mathbb{R}^n} \{g(\mathbf{x}) + r(\mathbf{x})\}, \quad (3)$$

where g is the data-fidelity term that quantifies the consistency with the measured data \mathbf{y} , and r is a regularizer that enforces a prior knowledge on the unknown image \mathbf{x} . For example, two widely-used data-fidelity and regularization terms in imaging are the least-squares and total variation (TV) terms:

$$g(\mathbf{x}) = \frac{1}{2} \|\mathbf{y} - \mathbf{A}\mathbf{x}\|_2^2 \quad \text{and} \quad r(\mathbf{x}) = \tau \|\mathbf{D}\mathbf{x}\|_1, \quad (4)$$

where $\tau > 0$ controls the regularization strength and \mathbf{D} denotes the discrete gradient operator [42]. Many handcrafted regularizers similar to TV have also been applied to sparse-view CT reconstruction problems [13, 43–47]. Beyond handcrafted priors, recent work has also explored the use of learned priors, e.g., [13, 18, 25, 27, 48].

DL has gained great popularity for solving CT inverse problems due to its excellent performance [49–51]. A widely used supervised DL approach is based on training a CNN to map a corrupted image to its clean target [52]. For example, prior work on DL for CBCT trains a CNN to map FBP reconstructed images to the corresponding ground-truth images. In particular, for CBCT where the target images are 3D, due to the memory limits, the network training is typically done in a slice-by-slice manner, where the 3D volumes are sliced into 2D images along a certain axes and the loss is optimized on the given slices [25, 27, 53, 54]. However, due to the lack of global information, a 2D slice-based approach cannot capture complex 3D structures as well as dedicated 3D reconstruction approaches [55]. An alternative method is to divide the whole volume into small 3D patches, feed the patches to the 3D network, and then fuse the reconstructed patches together (see reviews in [56]). While such 3D patch-based approach can extract and establish features in all dimensions within patches, it cannot model global correlations and the fusion of patches in forming the whole volume requires additional attention to boundary artifacts [57].

2.3 Our Contribution

This work contributes to the memory-expensive area of efficient 3D CBCT reconstruction using DL methods. We introduce a memory-efficient 2.5D network, called Swap-Net, that refines 3D images reconstructed from artifact-corrupted radiographs. Swap-Net addresses in an end-to-end fashion several common sources of

Table 1: Quantitative evaluation of Swap-Net and baseline methods averaged on the test dataset for different numbers of projection views. Swap-Net contains the fewest network parameters (PN) and uses moderate amount of GPU running memory (RM) yet achieved the highest SNR and SSIM compared with all the baseline methods across different projection settings.

Settings	Metric	PN (Million) / RM (GB)	AWGN						Scatter					
			SNR (dB)			SSIM			SNR (dB)			SSIM		
Views	—	—	4	8	16	4	8	16	4	8	16	4	8	16
FBP	—	—	9.04	13.19	15.53	0.63	0.68	0.72	9.44	11.57	12.03	0.64	0.7	0.75
TV	—	—	14.01	17.05	18.48	0.57	0.6	0.82	9.79	11.49	12.08	0.73	0.66	0.76
2D U-Net	50.26 / [0.77, 1.66]	—	20.77	20.93	20.94	0.95	0.95	0.95	17.01	17.77	20.30	0.89	0.91	0.95
3D U-Net	150.75 / [2.27, 9.25]	—	26.59	27.32	27.62	0.99	0.99	0.99	19.18	19.28	20.42	0.99	0.99	0.99
Swap-Net (Ours)	16.26 / [1.25, 5.91]	—	28.22	28.58	28.83	0.99	0.99	0.99	25.41	25.46	25.60	0.99	0.99	0.99

image artifacts, including those due to sparse view sampling, measurement noise, and photon scattering. We extensively test the performance of Swap-Net, validating that it can be used as an effective end-to-end mapping tool for 3D CBCT image reconstruction.

3 Proposed Method

We propose Swap-Net as an end-to-end mapping network that can handle 3D inverse problems like CBCT reconstruction. Fig. 1 shows the training pipeline (top) and architecture (bottom) of Swap-Net. As illustrated in the top part of Fig. 1, given the corrupted CBCT projections \mathbf{y} , Swap-Net R_θ takes the FBP reconstructed images $\mathbf{A}^\dagger \mathbf{y}$ as its input, and maps the whole volume to the desired 3D output $\hat{\mathbf{x}} := R_\theta(\mathbf{A}^\dagger \mathbf{y})$. Here, θ represents the parameters of Swap-Net, and \mathbf{A}^\dagger denotes the FBP reconstruction operation. Swap-Net training seeks to minimize the loss \mathcal{L} between $\hat{\mathbf{x}}$ and the ground truth \mathbf{x} over a training set consisting of J samples to obtain the optimized parameters θ^*

$$\theta^* = \arg \min_{\theta} \sum_{j=1}^J \mathcal{L}(\mathbf{x}_j, R_\theta(\mathbf{A}^\dagger \mathbf{y}_j)), \quad (5)$$

where \mathcal{L} denotes the loss function that measures the discrepancy between the predictions of the Swap-Net and the ground truth.

When the input images $\mathbf{A}^\dagger \mathbf{y}$ are of size $N_x \times N_y \times N_z$, Swap-Net works in a 3D-to-3D manner to produce a whole volume estimate $\hat{\mathbf{x}}$ having the same dimension as its input without slicing and assembling the volume. The efficiency of Swap-Net in facilitating 3D image reconstruction hinges upon the novel and efficient design of its architecture. As illustrated in the bottom part of Fig. 1, Swap-Net is a cascade of three repeating blocks, each consisting of two convolutional layers (Conv) followed by Rectified Linear Unit (ReLU) activations, one additional convolutional layer, and a residual connection. The convolutional kernels across all layers are uniformly set to a size of 3×3 with a stride of 1. The channel dimensions of the hidden convolutional layers are set to N_x , N_y , and N_z for the first, second, and final blocks, respectively, corresponding to the dimensions of the 3D input volume along the x , y , and z axes. A distinctive aspect of Swap-Net lies in its use of the *axes-swapping* operation after each block. This operation sequentially reorients the channel dimension to the x , y , and z axes, facilitating focused 2D convolutions across the yz , xz , and xy planes, respectively. This strategic approach enables the network to perform artifact reduction axis by axis, thereby ultimately yielding a high-fidelity 3D reconstruction that maintains consistency across all dimensions.

The key novelty of our method is that, to the best of our knowledge, this is the first work presenting such a memory-efficient 2.5D cascade network based on axes-swapping operations. Different from the traditional slice-by-slice mapping methods, Swap-Net instead relies on the axis-by-axis reconstruction, which can be particularly useful when the 3D volume is not uniformly corrupted along each dimension. For example, in CBCT imaging, since the projections are produced by rotating the X-ray beam along a certain axis, e.g., the z

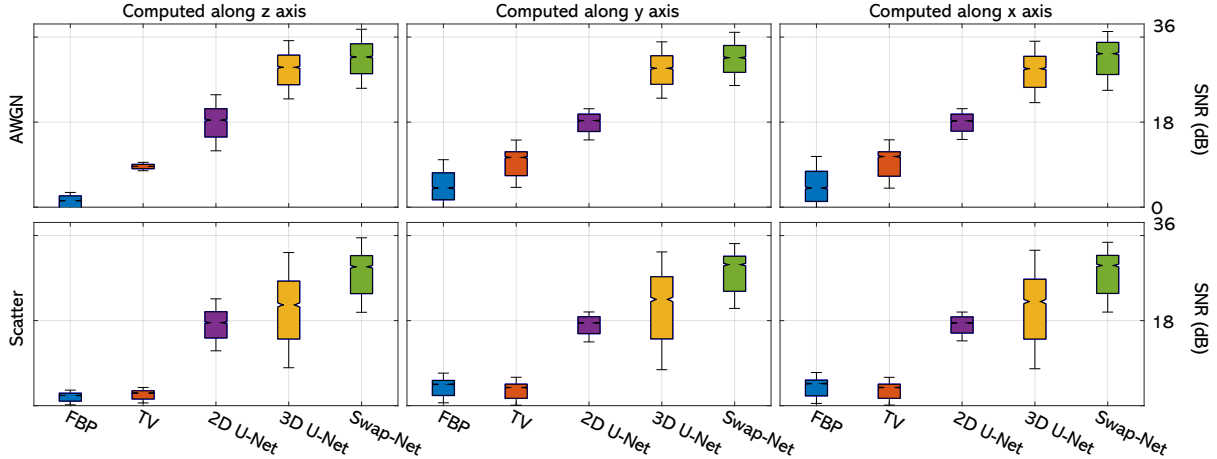


Figure 4: Statistical summary of SNR values for different reconstruction methods evaluated on 2D slices along each dimension taken from our test set. Plots in the first and second row correspond to the the results with 4 projection views under AWGN and non-ideal physics including blur and scatter and non-white noise corruptions, respectively.

axis in our experiments, the insufficient attenuation information along z usually leads to lower-quality images in the xy plane. The cascading axes-swapping operations in Swap-Net allow it to effectively process the reconstruction along axis z after accumulating more information along axis x and axis y , therefore enforcing the global consistency of the reconstructed 3D volume. Moreover, although the output of Swap-Net is the whole 3D volume, it does not involve any computationally expensive 3D convolutions. Instead, it is simply based on 2D convolutions where the convolution is looped over all axes of a 3D volume. Thus, Swap-Net overcomes the suboptimal performance of slice-based 2D CNNs that disregard the information across slices. On the other hand, it also bypasses the expensive computation cost of 3D networks, facilitating solving practical 3D imaging problems.

[t]

4 Experimental Validation

This section presents numerical results that demonstrate the ability of Swap-Net to provide high-quality 3D reconstructions from sparse-view 2D projections of ICF double-shell capsules as depicted in a representative double shell shown in Fig. 2. In particular, we examine Swap-Net under two different practical noise conditions, including AWGN corruption and nonlinear photon scattering corruption, to show its ability to solve challenging CBCT imaging problems.

4.1 Preparation of 3D Dataset

The emergence of Inertial Confinement Fusion (ICF) as a potential power source has been a major impetus for the continued examination of ICF implosion dynamics. One promising ICF configuration is a double-shell capsule, shown in Fig. 2 (a), that employs a high Z metallic shell that is imploded onto a gas-filled cavity via radiation to achieve fusion conditions. Both manufacturing as well as drive asymmetries may lead to hydrodynamic instabilities that can degrade ICF performance. Consequently, quantifying and understanding these instabilities is crucial to the continued success of ICF. To this end, radiography plays an essential

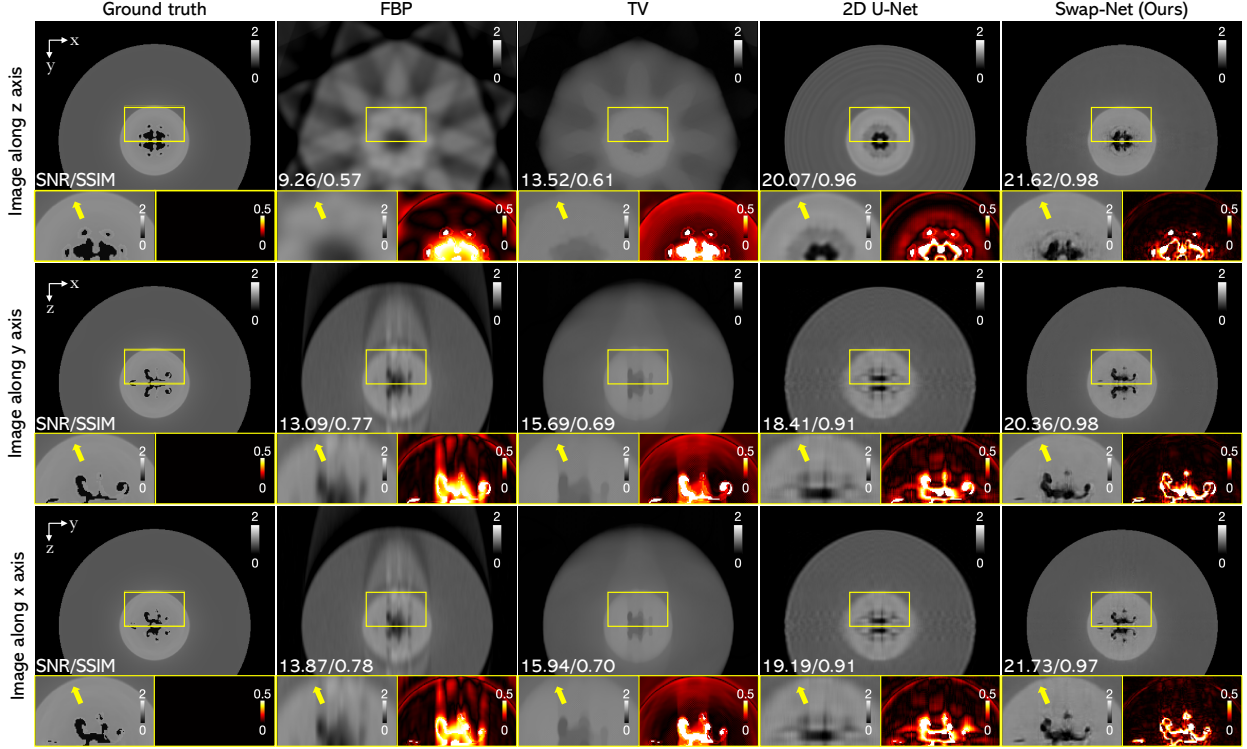


Figure 5: Visual evaluation of Swap-Net and baseline methods on an exemplar ICF double shell test simulation with 4 projection views under AWGN corruption. Each row shows the middle slice of the whole 3D object along z , y and x axes, respectively. The bottom part of each image provides the SNR and SSIM values and representative $2\times$ zoomed-in regions and their error maps with respect to the ground truth. Arrows in the zoomed-in plots highlight sharp edges that are well reconstructed using Swap-Net. Note the excellent quantitative and qualitative performance of Swap-Net for both artifact correction and detail preservation.

role in elucidating the behavior of the metallic shell and quantifying the impact of the asymmetries on ICF performance.

To further simplify the problem, we examine the implosion of a single shell made of tantalum, as this configuration enables the salient features to be captured in the density field, i.e., a complex gas metal interface without needing to increase the simulation complexity. As such we train and test our method with ICF capsules shown in Fig. 2 (b) to examine shock propagation and instability growth created using prescribed perturbations on the shell interior surface. All simulations were performed using computational fluid dynamics software.

In particular, our ICF capsules simulations were performed on a $440 \times 440 \times 440$ uniform Cartesian grid over $[0, L] \times [0, L] \times [0, L]$, where $L = 341 \mu\text{m}$. The uniform grid cell size is $\Delta x = \Delta y = \Delta z = \frac{440}{L}$. We used 108 3D objects with different parameters, e.g., initial 3D perturbations, material properties, and/or temporal slice where each case represents a distinct dynamic hydrodynamic configuration. Fig. 3 shows an exemplar object from our datasets with gas and tantalum labeled. In particular, the mass attenuation coefficient of gas is $\xi_{(\text{gas})} = 9.40 \text{ cm}^2/\text{g}$, and tantalum is $\xi_{(\text{tantalum})} = 13.03 \text{ cm}^2/\text{g}$, in the energy range of interest here. Each object has dimensions $448 \times 448 \times 448$ with voxel size $250 \times 250 \times 250 \mu\text{m}^3$. These 108 objects were split into 90, 18, and 18 for training, validation, and testing, respectively.

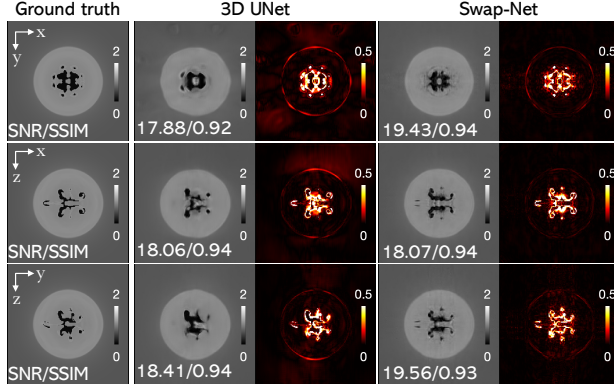


Figure 6: Visual evaluation of 2.5D Swap-Net and 3D U-Net on an exemplar ICF double shell test simulation with 4 projection views under AWGN corruption. Each row shows the middle slice of the central region of the 3D object and the corresponding error maps with respect to the ground truth along z , y and x axes, respectively. The bottom part of each image provides the SNR and SSIM values. With only about 1/10 of the parameters of 3D U-Net, Swap-Net still achieves better quantitative and qualitative performance.

4.2 Generation of Radiographs

The direct radiographic signals from the area mass were simulated by rotating the X-ray source along axis z with base intensity $I_0 = 3.201 \times 10^{-4}$. We tested the performance of Swap-Net on sparse-view CBCT reconstruction with 4, 8 and 16 views. The dimensions of the 2D projections were 200×200 with resolution $2000 \times 2000 \mu\text{m}^2$. These CBCT views were generated using the ODL package [58], and all views were equally spaced over 180 degrees.

We generated the radiographs under two different corruption scenarios, namely AWGN, as modeled in (1), and non-ideal physics including blur and scatter and non-white noise corruption, as modeled in (2), respectively. For AWGN, the simulated corrupted radiographs included the addition of random AWGN corresponding to an input SNR of 40dB to the clean ones. For our non-idea physics investigation, we modeled the total transmission or the noisy radiograph function Φ as the sum of the blurred radiograph, scatter, and noise as follows:

$$\Phi := D_{\text{blur}} + D_s + B_s + \eta. \quad (6)$$

Let D denote the uncollided radiation incident on the detector plane. The blurred direct radiation component is given by

$$D_{\text{blur}} = D * G_{\text{blur}}(\sigma_{\text{blur}}) * \phi_{\text{db}}. \quad (7)$$

The source blur G_{blur} is given by a 2D Gaussian kernel with deviation σ_{blur} chosen randomly between 1 and 3 pixels with an accompanying random orientation between 5 and 26 degrees. This signal was then convolved with a detector blur using another kernel ϕ_{db} .

To address the scatter radiation, we included two scatter components. The first was a correlated scatter component given by

$$D_s = \kappa D * G_{\text{scatter}}(\sigma_{\text{scatter}}). \quad (8)$$

Here we convolved the direct radiograph with a 2D Gaussian filter scatter kernel G_{scatter} having standard deviation σ_{scatter} between 10 and 30 pixels for the kernel, with a scaling factor κ between 0.1 and 0.3. We also added a background scatter field B_s , which is another essential component of scatter affecting radiographic measurements. Physically, this term represents scatter from our object that is reflected by nearby surrounding objects, e.g., ground and walls, which are particularly difficult to model. This field was modeled with a

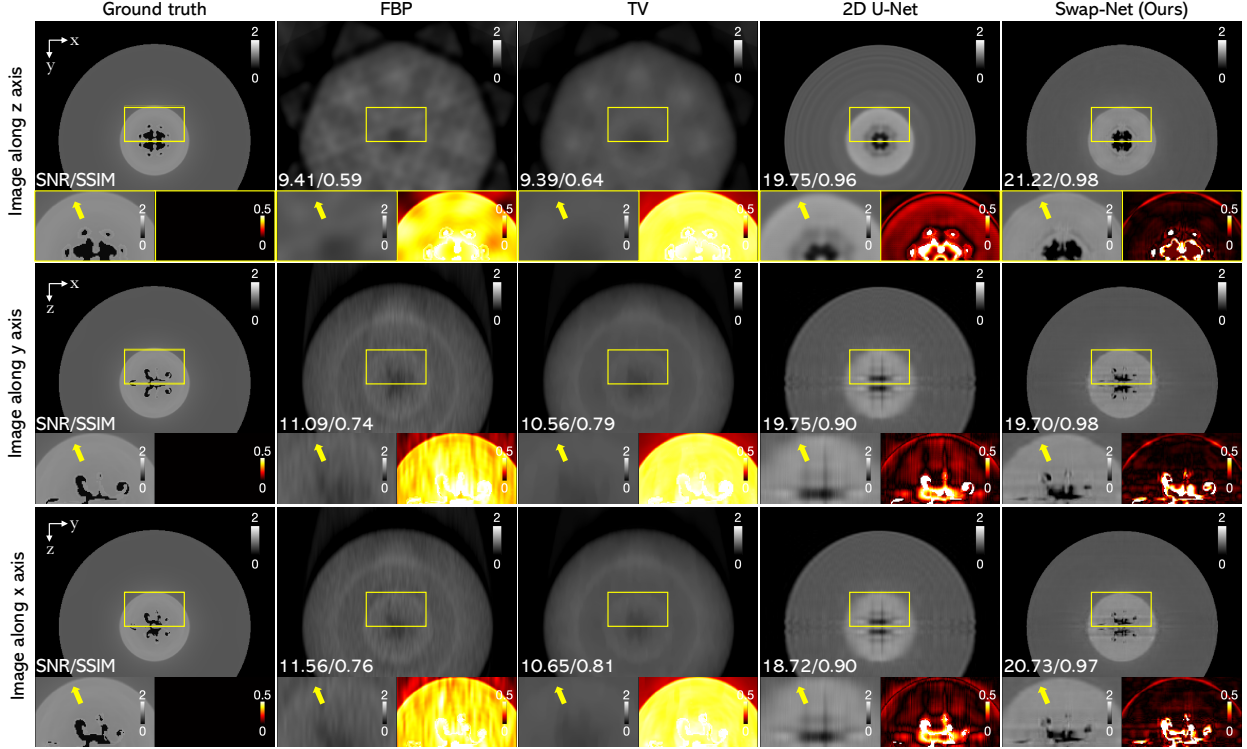


Figure 7: Visual evaluation of Swap-Net and baseline methods on an exemplar ICF double shell test simulation with 4 projection views under scatter corruption. Each row shows the middle slice of the whole 3D object along z , y and x axes, respectively. The bottom part of each image provides the SNR and SSIM values, and representative $2\times$ zoomed-in regions and their error maps with respect to the ground truth. Arrows in the zoomed-in plots highlight sharp edges that are well reconstructed using Swap-Net. Note the excellent quantitative and qualitative performance of Swap-Net for both artifacts correction and detail preservation.

polynomial of order n given as

$$B_s(x, y) = \sum_{i=0}^n a_i x^i + b_i y^i, \quad (9)$$

where x and y denote spatial coordinates and a_i and b_i denote the coefficients of the polynomial. We chose the coefficients of the background scatter field such that the level was randomly between 0.5 and 1.5 times the mean signal level in the center of the image and the tilt was between -10% and 10%.

We modeled gamma and photon noise as Poisson noise denoted by η_g^{Po} and η_p^{Po} , respectively. The means of the two distributions were proportional to the total signal $D_{\text{blur}} + D_s + B_s$ (with a scaling for each noise). The noise components were convolved with respective kernels ϕ_g and ϕ_p to give the total (colored) noise η as follows:

$$\eta = \kappa_g(\eta_g^{\text{Po}} * \phi_g) + \kappa_p(\eta_p^{\text{Po}} * \phi_p), \quad (10)$$

where κ_g and κ_p are scaling coefficients for the gamma and photon noise components, respectively. The level of the gamma noise was randomly set in the range of (39,000, 50,000) and the level of the photon noise was randomly set in the range (350, 450). All random parameters were generated independently for each radiograph, so each radiograph was corrupted with different random noise and scatter realizations.

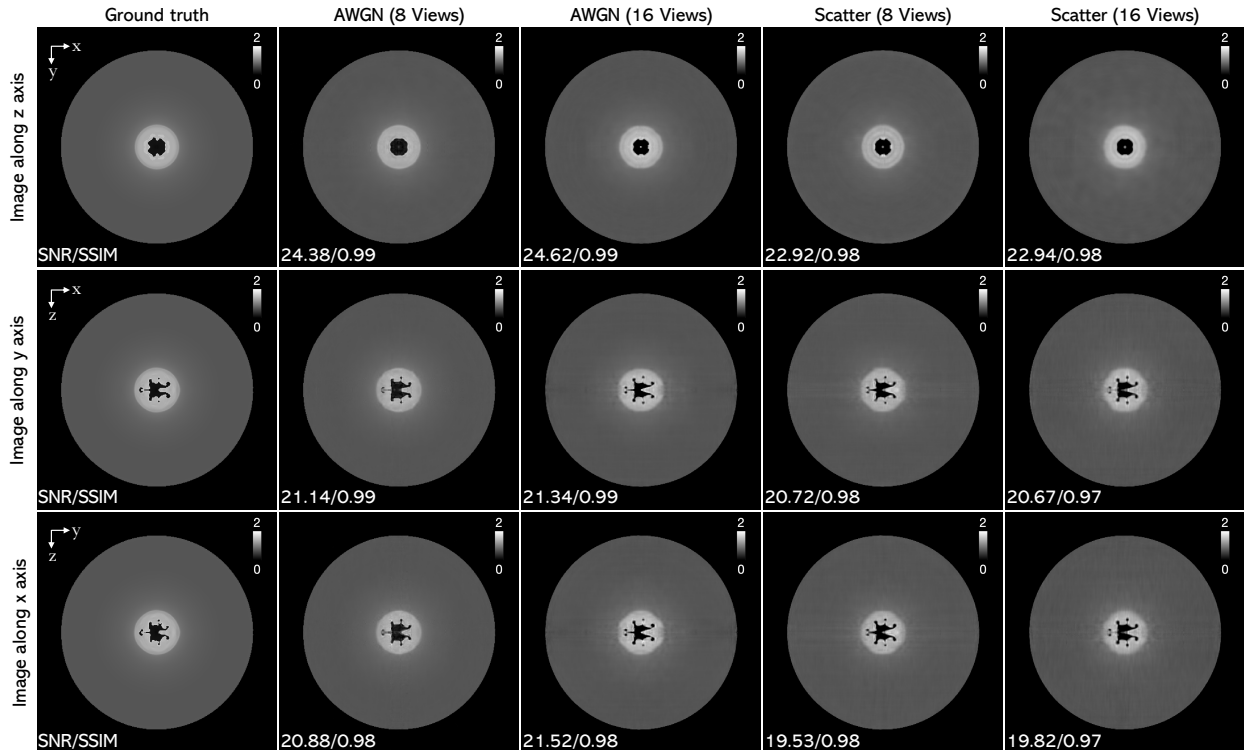


Figure 8: Visual evaluation of Swap-Net on an exemplar ICF double shell test simulation with 8 and 16 projections views under AWGN and non-ideal physics including blur and scatter and non-white noise (labeled as Scatter) corruptions. Each row shows the middle slice of the whole 3D object along z , y and x axes, respectively. The bottom-left corner of each image provides the SNR and SSIM values with respect to the ground truth. Note the consistently good performance of Swap-Net for different projection views and noise corruptions.

4.3 Baseline Methods and Training Settings

We considered several well-known algorithms as baseline methods for CBCT image reconstruction, including *FBP*, *TV* [42], *2D U-Net* [59], and *3D U-Net* [60]. *FBP* and *TV* are traditional methods that do not require training, while other methods are all DL methods with publicly available implementations. The *FBP* method was performed with the Hann filter, and the relative cutoff frequency for the filter was set to 0.3. We used `fminbound` in the `scipy.optimize` toolbox to identify the optimal regularization parameter τ for *TV* at the inference time. We trained all DL methods on the *FBP* reconstructed images to handle CBCT reconstruction. For *3D U-Net*, we trained the model with 3D patches with patch size set to $112 \times 112 \times 112$, and fused patches to form its final reconstruction. We used the ℓ_2 loss function for all training approaches, and set the learning rate to 0.001 and used Adam [61] as our training optimizer. All models were trained for 1000 epochs, at which point stable convergence was observed. We evaluated reconstruction performance using two widely-adopted metrics: signal to noise ration (SNR) in dB and structural similarity index measure (SSIM) from `skimage.metrics` toolbox. Models that achieved the best performance on our validation dataset were selected for inference.

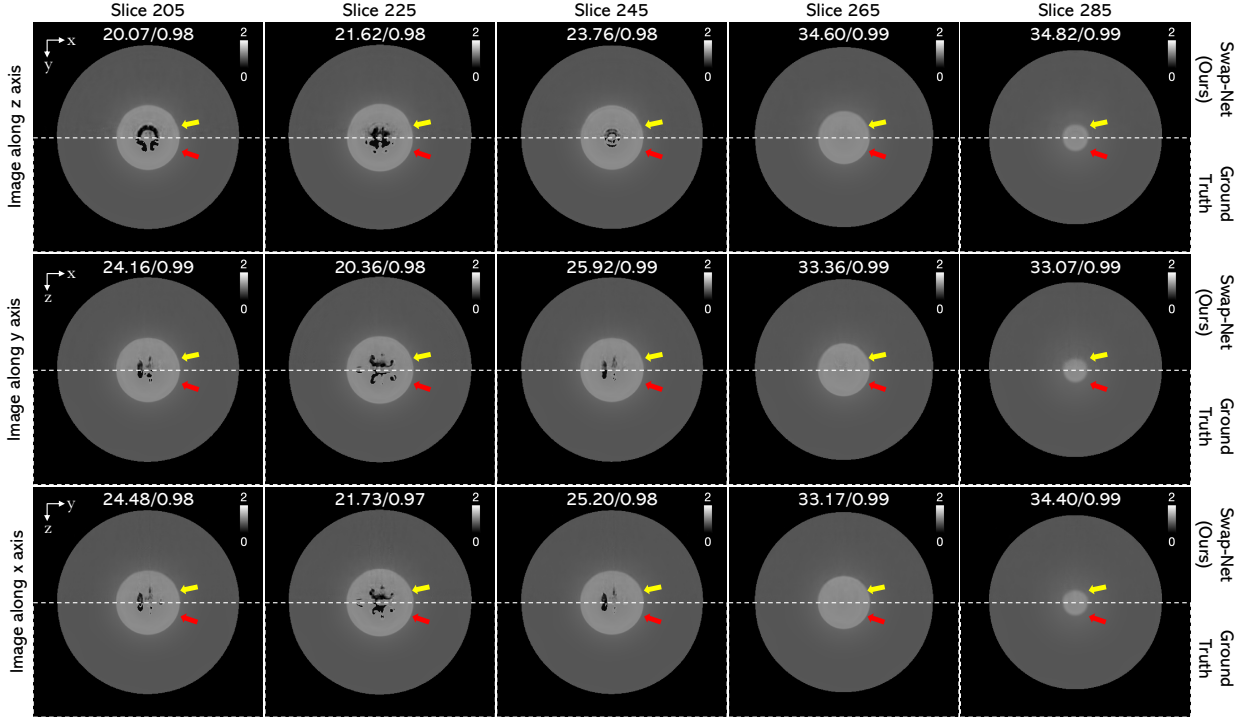


Figure 9: Visual evaluation of Swap-Net across different slices on an exemplar ICF double shell test simulation with 4 projection views under AWGN corruption. Each row shows different slices of the whole 3D object along z , y and x axes, respectively. In each row, the images to the top of the dashed line are the reconstructed images from Swap-Net, while the images to the bottom are ground truth. The top-middle part of each image provides the SNR and SSIM values with respect to the ground truth. Arrows in the plots highlight sharp edge regions that are well reconstructed using Swap-Net. Note the consistently good performance of Swap-Net across different slices of a 3D object.

4.4 Results and Analysis

We first compared the performance of Swap-Net with baseline methods. Table 1 summarizes the averaged quantitative evaluation of Swap-Net and baseline methods on our testing dataset with different numbers of projection views. These numerical results were evaluated on the whole 3D volume for both AWGN corruption and non-ideal physics including blur and scatter and photon noise corruption. Swap-Net consistently outperformed the baseline methods, leading to the best SNR and SSIM in different scenarios. As a reference for model complexity, Table 1 also presents the model size in terms of the number of parameters (PN). Despite obtaining significantly enhanced performance, Swap-Net only uses about 1/3 as many parameters as 2D U-Net and 1/10 as many parameters as 3D U-Net. We also reported the GPU running memory (RM) usage¹ in table 1. Note that Swap-Net processes the entire 3D volume during training, whereas the patch-based 3D U-Net processes 1/64 of the volume, and the slice-based 2D U-Net processes 1/448 of the volume. Despite these differences in data-related RM demands, Swap-Net’s overall RM usage is still lower than that of the 3D U-Net and only slightly higher than the 2D U-Net, making it a memory-efficient solution in practice. To further evaluate the performance of the reconstruction along each of dimension of the 3D object, Fig. 4 summarizes the statistical evaluation for slice-wise reconstruction for both AWGN corruption and non-ideal

¹The RM usage is presented in the format of [averaged running GPU memory usage, peak running GPU memory usage]. The RM usage for each model were computed by running experiments with batch size of 1 and projection views of 4.

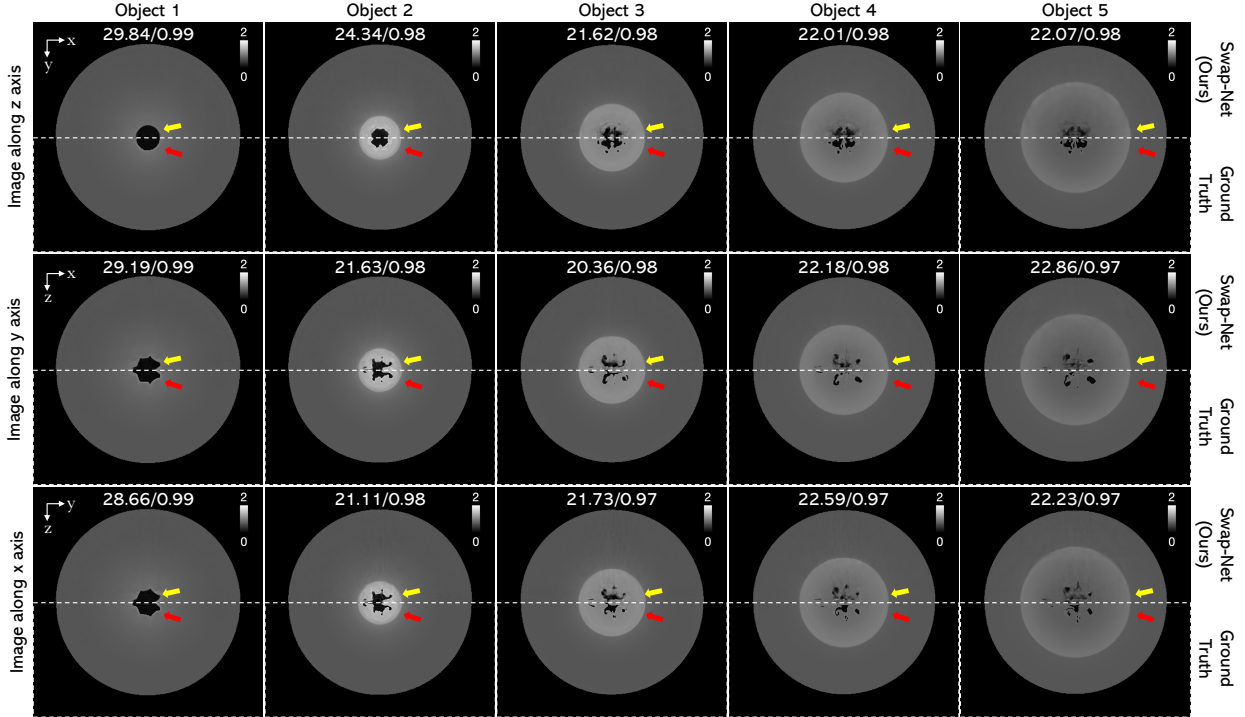


Figure 10: Visual evaluation of Swap-Net on different exemplar ICF double shell test simulations with 4 projection views under AWGN corruption. Each row shows different slices of the whole 3D object along z , y and x axes, respectively. In each row, the images above the dashed line are the images reconstructed from Swap-Net, while the images below are the ground truth. The top-middle part of each image provides the SNR and SSIM values with respect to the ground truth. Arrows in the plots highlight sharp edge regions that are well reconstructed using Swap-Net. Swap-Net had consistently good performance across different 3D objects.

physics including blur and scatter and photon noise corruptions. Swap-Net achieved consistently good reconstruction performance for 2D image slices along all three dimensions, thanks to the axes-swapping operation in our network design.

Fig. 5 presents visual comparisons from different methods on an exemplar testing data under AWGN corruption with 4 views. Swap-Net outperformed the baseline methods both in terms of removing artifacts and maintaining sharpness. The excellent performance demonstrates that Swap-Net can remove disturbing artifacts while retaining detailed structural information. Such capability is notable for a network having only 9 convolution layers. Because the CBCT projections were simulated by rotating along the z axis, it is challenging to reconstruct images along z especially with sparse-view projections (e.g., see the comparatively worse FBP reconstruction in (x, y) plane in Fig. 5). Swap-Net overcomes such asymmetric artifacts by performing cascading convolutions along all axes, resulting in the comparatively consistent reconstruction along all dimensions. Fig. 6 compares Swap-Net and 3D patch-based U-Net methods; to avoid the influence of the edge artifacts, only the central region of the reconstructed object is presented. In Fig. 6, Swap-Net performed better than the 3D U-net. Fig. 7 demonstrates the improved performance of Swap-Net compared with various baseline methods under non-ideal physics including blur and scatter and photon noise corruption. While the baseline methods obviously suffer from scatter corruption, Swap-Net successfully reduced the artifacts, leading to a similar good quantitative and qualitative performance as in the AWGN case. Fig. 8 presents the results of additional investigations with the baseline methods using 8 and 16 views.

Fig. 9 further illustrates the performance of Swap-Net across different slices in a whole 3D object volume.

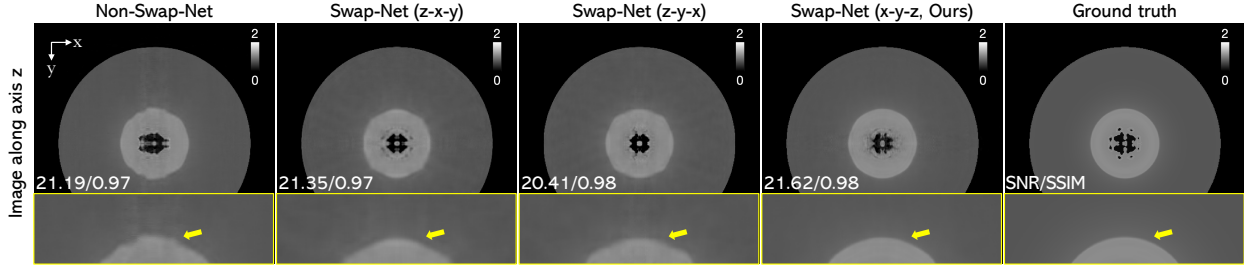


Figure 11: Quantitative and visual evaluation of Swap-Net variants with different axes-swapping settings on an exemplar ICF double shell test simulation with 4 projection views under AWGN corruption. The middle slice of the whole 3D object along z axis is plotted. The bottom-left corner of each image provides the SNR and SSIM values, and $2\times$ zoomed-in region. Arrows in the zoomed-in plots highlight sharp edges that are well reconstructed using Swap-Net with swapping order $x-y-z$. Note the the improvement from non-Swap-Net to Swap-Net variants, and the the influence of the order of axes-swapping operations in the reconstruction.

For each slice, we show the side-to-side (top versus bottom) comparison between the results of Swap-Net and the corresponding ground truth. Using only 4 projection views, Swap-Net successfully reconstructed not only the sharp edges but also central details, matching well with the ground truth. The consistent success of Swap-Net on different slices suggests that it can work across the 3D volume, highlighting its effectiveness and adaptability. Fig. 10 additionally shows the visual performance of Swap-Net for different objects.

4.5 Additional Study

To highlight the contribution of Swap-Net’s axes-swapping operation, we performed an additional study to examine its influence. First, we investigated a *Non-Swap-Net* network identical to the Swap-Net but without the axes-swapping operations. Comparing to Non-Swap-Net helps to illustrate improvements due to axes-swapping operations. We also tested Swap-Net with different axes-swapping orders. Letting z denote the CBCT rotation axis, we checked the the following axes-swapping orders: (a) $z-x-y$, (b) $x-z-y$, and (c) $x-y-z$, namely putting the convolution in the xy plane in the beginning, middle, and end of the Swap-Net pipeline. Order (c) $x-y-z$ is the strategy adopted in our paper. Fig. 11 presents the reconstruction performance of those Swap-Net variants; it shows z -axis slices (similar results were observed for images along x and y axes and therefore were omitted here). Clearly, Non-Swap-Net gave the worst results with obvious artifacts, and Swap-Net with axes-swapping orders of $z-x-y$ and $x-z-y$ did not perform as well as the $x-y-z$ order. We hypothesize this is because the relative worse FBP reconstruction along the z axis makes the learning along z more challenging, so putting the convolution along z at the end of the Swap-Net pipeline allows it to exploit the intermediate object reconstruction.

5 Conclusion

This paper presents a memory-efficient 2.5D network, namely Swap-Net, for handling 3D image reconstruction problems like sparse-view CBCT. The major challenge in this problem is to reconstruct high-quality 3D images efficiently and accurately when only a limited number of projections and training data are available, and when complicated corruptions are presented. Swap-Net uses a novel axes-swapping operation that allows for sequential convolution along all three dimension of a 3D object. We optimized the network weights by minimizing the loss between the output of the Swap-Net and the ground-truth 3D images on the training dataset using FBP reconstruction as inputs. We demonstrated the enhanced performance of our method on sparse-view 3D CBCT image reconstruction relative to model-based regularization (such as TV), 2D, and 3D

CNNs under both AWGN and non-ideal physics including blur and scatter and photon noise corruptions. Our extensive validation elaborated the potential of Swap-Net on producing high-quality images from artifact-corrupted measurements. Although this paper focuses on CBCT reconstruction, our network can be extended to other 3D imaging applications.

In conclusion, our method exploits the lower computational cost of 2D convolution while bridging the gap to 3D convolution via axes-swapping operations, thereby offering a computationally efficient strategy for handling memory-demanding 3D reconstructions. Further improvement may be possible by increasing the depth of each convolution block in Swap-Net. This work kept the channel dimension to be the same value for all Swap-Net blocks for simplicity; future work could optimize the feature dimensions. It could also be interesting to explore connections between Swap-Net and tensor decomposition methods, e.g., [62]. Applying Swap-Net to other imaging tasks is planned in the near future.

6 Acknowledgement

Acknowledgment: This work was supported by the U.S. Department of Energy through Los Alamos National Laboratory (LANL). The authors acknowledge Jennifer Schei Disterhaupt from LANL for contributing to the code for the noise and scatter model. The authors would also like to thank Robert Reinovsky (LANL) for his support of the project.

Data availability statement: Data underlying the results presented in this paper are not publicly available at this time but may be obtained from the authors upon reasonable request.

Disclosures statement: The authors declare no conflicts of interest.

References

- [1] T. Selig, T. Marz, M. Storath, and A. Weinmann, “Low-dose CT image reconstruction by fine-tuning a UNet pretrained for Gaussian denoising for the downstream task of image enhancement,” 2024. [Online]. Available: <http://arxiv.org/abs/2403.03551>
- [2] H. M. Alamri, M. Sadrameli, M. A. Alshalhoob, and M. A. Alshehri, “Applications of cbct in dental practice: a review of the literature.” *General dentistry*, vol. 60, no. 5, pp. 390–400, 2012.
- [3] K. Horner, L. O’Malley, K. Taylor, and A.-M. Glennly, “Guidelines for clinical use of cbct: a review,” *Dentomaxillofacial radiology*, vol. 44, no. 1, p. 20140225, 2015.
- [4] J. Casselman, K. Gieraerts, D. Volders, J. Delanote, K. Mermuys, B. De Foer, and G. Swennen, “Cone beam ct: non-dental applications,” *Journal of the Belgian Society of Radiology*, vol. 96, no. 6, pp. 333–353, 2013.
- [5] L. A. Feldkamp, L. C. Davis, and J. W. Kress, “Practical cone beam algorithm,” *J. Opt. Soc. Am. A*, vol. 1, no. 6, pp. 612–9, Jun. 1984.
- [6] X. Pan, E. Y. Sidky, and M. Vannier, “Why do commercial ct scanners still employ traditional, filtered back-projection for image reconstruction?” *Inverse problems*, vol. 25, no. 12, p. 123009, 2009.
- [7] K. Sauer and C. Bouman, “A local update strategy for iterative reconstruction from projections,” *IEEE Transactions on Signal Processing*, vol. 41, no. 2, pp. 534–548, 1993.
- [8] K. Kim, J. C. Ye, W. Worstell, J. Ouyang, Y. Rakvongthai, G. El Fakhri, and Q. Li, “Sparse-view spectral ct reconstruction using spectral patch-based low-rank penalty,” *IEEE transactions on medical imaging*, vol. 34, no. 3, pp. 748–760, 2014.
- [9] J. A. Fessler, M. Sonka, and J. M. Fitzpatrick, “Statistical image reconstruction methods for transmission tomography,” *Handbook of medical imaging*, vol. 2, pp. 1–70, 2000.

- [10] I. A. Elbakri and J. A. Fessler, "Statistical image reconstruction for polyenergetic x-ray computed tomography," *IEEE transactions on medical imaging*, vol. 21, no. 2, pp. 89–99, 2002.
- [11] J.-B. Thibault, C. A. Bouman, K. D. Sauer, and J. Hsieh, "A recursive filter for noise reduction in statistical iterative tomographic imaging," in *Computational Imaging IV*, vol. 6065. SPIE, 2006, pp. 264–273.
- [12] M. Beister, D. Kolditz, and W. A. Kalender, "Iterative reconstruction methods in x-ray ct," *Physica medica*, vol. 28, no. 2, pp. 94–108, 2012.
- [13] C. Zhang, T. Zhang, M. Li, C. Peng, Z. Liu, and J. Zheng, "Low-dose ct reconstruction via l1 dictionary learning regularization using iteratively reweighted least-squares," *Biomedical engineering online*, vol. 15, pp. 1–21, 2016.
- [14] W. Yu, C. Wang, X. Nie, M. Huang, and L. Wu, "Image reconstruction for few-view computed tomography based on l0 sparse regularization," *Procedia Computer Science*, vol. 107, pp. 808–813, 2017.
- [15] C. Xu, B. Yang, F. Guo, W. Zheng, and P. Poignet, "Sparse-view cbct reconstruction via weighted Schatten p-norm minimization," *Optics Express*, vol. 28, no. 24, pp. 35 469–35 482, 2020.
- [16] R. Anirudh, H. Kim, J. J. Thiagarajan, K. A. Mohan, K. Champley, and T. Bremer, "Lose the views: Limited angle ct reconstruction via implicit sinogram completion," in *Proceedings of the IEEE Conference on Computer Vision and Pattern Recognition*, 2018, pp. 6343–6352.
- [17] S. Ravishankar, J. C. Ye, and J. A. Fessler, "Image reconstruction: From sparsity to data-adaptive methods and machine learning," *Proceedings of the IEEE*, vol. 108, no. 1, pp. 86–109, 2019.
- [18] X. Zheng, S. Ravishankar, Y. Long, and J. A. Fessler, "Pwls-ultra: An efficient clustering and learning-based approach for low-dose 3d ct image reconstruction," *IEEE transactions on medical imaging*, vol. 37, no. 6, pp. 1498–1510, 2018.
- [19] H. Chen, Y. Zhang, Y. Chen, J. Zhang, W. Zhang, H. Sun, Y. Lv, P. Liao, J. Zhou, and G. Wang, "Learn: Learned experts' assessment-based reconstruction network for sparse-data ct," *IEEE transactions on medical imaging*, vol. 37, no. 6, pp. 1333–1347, 2018.
- [20] H. Gupta, K. H. Jin, H. Q. Nguyen, M. T. McCann, and M. Unser, "Cnn-based projected gradient descent for consistent ct image reconstruction," *IEEE transactions on medical imaging*, vol. 37, no. 6, pp. 1440–1453, 2018.
- [21] J. R. Hershey, J. L. Roux, and F. Weninger, "Deep unfolding: Model-based inspiration of novel deep architectures," *arXiv preprint arXiv:1409.2574*, 2014.
- [22] V. Monga, Y. Li, and Y. C. Eldar, "Algorithm unrolling: Interpretable, efficient deep learning for signal and image processing," *IEEE Signal Processing Magazine*, vol. 38, no. 2, pp. 18–44, 2021.
- [23] A. Hauptmann, F. Lucka, M. Betcke, N. Huynh, J. Adler, B. Cox, P. Beard, S. Ourselin, and S. Arridge, "Model-based learning for accelerated, limited-view 3-D photoacoustic tomography," *IEEE Trans. Med. Imag.*, vol. 37, no. 6, pp. 1382–1393, 2018.
- [24] J. Adler and O. Öktem, "Learned primal-dual reconstruction," *IEEE Trans. Med. Imag.*, vol. 37, no. 6, pp. 1322–1332, Jun. 2018.
- [25] J. Liu, Y. Sun, W. Gan, X. Xu, B. Wohlberg, and U. S. Kamilov, "Sgd-net: Efficient model-based deep learning with theoretical guarantees," *IEEE Transactions on Computational Imaging*, vol. 7, pp. 598–610, 2021.
- [26] S. Mukherjee, M. Carioni, O. Öktem, and C.-B. Schönlieb, "End-to-end reconstruction meets data-driven regularization for inverse problems," in *Advances in Neural Information Processing Systems*, vol. 34. Curran Associates, Inc., 2021, pp. 21 413–21 425.

- [27] J. Liu, X. Xu, W. Gan, U. Kamilov *et al.*, “Online deep equilibrium learning for regularization by denoising,” *Advances in Neural Information Processing Systems*, vol. 35, pp. 25 363–25 376, 2022.
- [28] D. Wu, K. Kim, G. El Fakhri, and Q. Li, “Iterative low-dose ct reconstruction with priors trained by artificial neural network,” *IEEE transactions on medical imaging*, vol. 36, no. 12, pp. 2479–2486, 2017.
- [29] I. Y. Chun, Z. Huang, H. Lim, and J. A. Fessler, “Momentum-net: Fast and convergent iterative neural network for inverse problems,” *IEEE transactions on pattern analysis and machine intelligence*, vol. 45, no. 4, pp. 4915–4931, 2020.
- [30] B. Zhou, S. K. Zhou, J. S. Duncan, and C. Liu, “Limited view tomographic reconstruction using a cascaded residual dense spatial-channel attention network with projection data fidelity layer,” *IEEE transactions on medical imaging*, vol. 40, no. 7, pp. 1792–1804, 2021.
- [31] Y. Huang, A. Preuhs, G. Lauritsch, M. Manhart, X. Huang, and A. Maier, “Data consistent artifact reduction for limited angle tomography with deep learning prior,” in *International workshop on machine learning for medical image reconstruction*. Springer, 2019, pp. 101–112.
- [32] S. Lee, H. Chung, M. Park, J. Park, W.-S. Ryu, and J. C. Ye, “Improving 3d imaging with pre-trained perpendicular 2d diffusion models,” in *Proceedings of the IEEE/CVF International Conference on Computer Vision (ICCV)*, October 2023, pp. 10 710–10 720.
- [33] A. Yuniarti and N. Suciati, “A review of deep learning techniques for 3d reconstruction of 2d images,” in *2019 12th International Conference on Information & Communication Technology and System (ICTS)*, 2019, pp. 327–331.
- [34] E. C. Merritt, J. P. Sauppe, E. N. Loomis, T. Cardenas, D. S. Montgomery, W. S. Daughton, D. C. Wilson, J. L. Kline, S. F. Khan, M. Schoff *et al.*, “Experimental study of energy transfer in double shell implosions,” *Physics of Plasmas*, vol. 26, no. 5, 2019.
- [35] J.-B. Thibault, K. D. Sauer, C. A. Bouman, and J. Hsieh, “A three-dimensional statistical approach to improved image quality for multislice helical ct,” *Medical physics*, vol. 34, no. 11, pp. 4526–4544, 2007.
- [36] J. A. Fessler, “Model-based image reconstruction for mri,” *IEEE Signal Processing Magazine*, vol. 27, no. 4, pp. 81–89, 2010.
- [37] M. Sun and J. M. Star-Lack, “Improved scatter correction using adaptive scatter kernel superposition,” *Physics in Medicine and Biology*, vol. 55, no. 22, pp. 6695–6720, Oct. 2010.
- [38] M. T. McCann, M. L. Klasky, J. L. Schei, and S. Ravishankar, “Local models for scatter estimation and descattering in polyenergetic X-ray tomography,” *Opt. Express*, vol. 29, no. 18, pp. 29 423–29 438, 2021.
- [39] A. H. Delaney and Y. Bresler, “Globally convergent edge-preserving regularized reconstruction: an application to limited-angle tomography,” *IEEE Transactions on Image Processing*, vol. 7, no. 2, pp. 204–221, 1998.
- [40] D. F. Yu and J. A. Fessler, “Edge-preserving tomographic reconstruction with nonlocal regularization,” *IEEE transactions on medical imaging*, vol. 21, no. 2, pp. 159–173, 2002.
- [41] M. Pasha, A. K. Saibaba, S. Gazzola, M. I. Español, and E. de Sturler, “A computational framework for edge-preserving regularization in dynamic inverse problems,” *Electronic Transactions on Numerical Analysis*, vol. 58, pp. 486–516, 2023.
- [42] L. I. Rudin, S. Osher, and E. Fatemi, “Nonlinear total variation based noise removal algorithms,” *Physica D*, vol. 60, no. 1–4, pp. 259–268, Nov. 1992.
- [43] E. Y. Sidky, C.-M. Kao, and X. Pan, “Accurate image reconstruction from few-views and limited-angle data in divergent-beam ct,” *Journal of X-ray Science and Technology*, vol. 14, no. 2, pp. 119–139, 2006.

- [44] G. T. Herman and R. Davidi, "Image reconstruction from a small number of projections," *Inverse problems*, vol. 24, no. 4, p. 045011, 2008.
- [45] G.-H. Chen, J. Tang, and S. Leng, "Prior image constrained compressed sensing (piccs): a method to accurately reconstruct dynamic ct images from highly undersampled projection data sets," *Medical physics*, vol. 35, no. 2, pp. 660–663, 2008.
- [46] J. Bian, J. H. Siewerdsen, X. Han, E. Y. Sidky, J. L. Prince, C. A. Pelizzari, and X. Pan, "Evaluation of sparse-view reconstruction from flat-panel-detector cone-beam ct," *Physics in Medicine & Biology*, vol. 55, no. 22, p. 6575, 2010.
- [47] S. Ramani and J. A. Fessler, "A splitting-based iterative algorithm for accelerated statistical x-ray ct reconstruction," *IEEE transactions on medical imaging*, vol. 31, no. 3, pp. 677–688, 2011.
- [48] L. Pfister and Y. Bresler, "Model-based iterative tomographic reconstruction with adaptive sparsifying transforms," in *Computational Imaging XII*, vol. 9020. SPIE, 2014, pp. 125–135.
- [49] J. Dong, J. Fu, and Z. He, "A deep learning reconstruction framework for x-ray computed tomography with incomplete data," *PloS one*, vol. 14, no. 11, p. e0224426, 2019.
- [50] H. Kim, R. Anirudh, K. A. Mohan, and K. Champley, "Extreme few-view ct reconstruction using deep inference," *arXiv preprint arXiv:1910.05375*, 2019.
- [51] J. C. Montoya, C. Zhang, Y. Li, K. Li, and G.-H. Chen, "Reconstruction of three-dimensional tomographic patient models for radiation dose modulation in ct from two scout views using deep learning," *Medical physics*, vol. 49, no. 2, pp. 901–916, 2022.
- [52] K. H. Jin, M. T. McCann, E. Froustey, and M. Unser, "Deep convolutional neural network for inverse problems in imaging," *IEEE Trans. Im. Proc.*, vol. 26, no. 9, pp. 4509–22, Sep. 2017.
- [53] Y. Han, J. Kang, and J. C. Ye, "Deep learning reconstruction for 9-view dual energy ct baggage scanner," *arXiv preprint arXiv:1801.01258*, 2018.
- [54] S. Guan, A. A. Khan, S. Sikdar, and P. V. Chitnis, "Limited-view and sparse photoacoustic tomography for neuroimaging with deep learning," *Scientific reports*, vol. 10, no. 1, p. 8510, 2020.
- [55] X. Xu, S. V. Kothapalli, J. Liu, S. Kahali, W. Gan, D. A. Yablonskiy, and U. S. Kamilov, "Learning-based motion artifact removal networks for quantitative r2* mapping," *Magnetic resonance in medicine*, vol. 88, no. 1, pp. 106–119, 2022.
- [56] D. Karimi and R. K. Ward, "Patch-based models and algorithms for image processing: a review of the basic principles and methods, and their application in computed tomography," *International journal of computer assisted radiology and surgery*, vol. 11, pp. 1765–1777, 2016.
- [57] S. Majee, T. Balke, C. A. Kemp, G. T. Buzzard, and C. A. Bouman, "4d x-ray ct reconstruction using multi-slice fusion," in *2019 IEEE International Conference on Computational Photography (ICCP)*. IEEE, 2019, pp. 1–8.
- [58] J. Adler, H. Kohr, and O. Öktem, "Operator discretization library (odl)," Jan. 2017. [Online]. Available: <https://doi.org/10.5281/zenodo.249479>
- [59] O. Ronneberger, P. Fischer, and T. Brox, "U-Net: Convolutional networks for biomedical image segmentation," in *Medical Image Computing and Computer-Assisted Intervention (MICCAI)*, Munich, Germany, Oct. 2015, pp. 234–241.

- [60] Ö. Çiçek, A. Abdulkadir, S. S. Lienkamp, T. Brox, and O. Ronneberger, “3d u-net: learning dense volumetric segmentation from sparse annotation,” in *Medical Image Computing and Computer-Assisted Intervention–MICCAI 2016: 19th International Conference, Athens, Greece, October 17-21, 2016, Proceedings, Part II 19*. Springer, 2016, pp. 424–432.
- [61] D. Kingma and J. Ba, “Adam: A method for stochastic optimization,” in *International Conference on Learning Representations (ICLR)*, San Diego, CA, USA, May 2015, pp. 1–13.
- [62] M. E. Kilmer, L. Horesh, H. Avron, and E. Newman, “Tensor-tensor algebra for optimal representation and compression of multiway data,” *Proceedings of the National Academy of Sciences*, vol. 118, no. 28, p. e2015851118, 2021.